Linking terrestrial biogeochemical processes and water ages to catchment water quality: A new Damköhler analysis based on coupled modeling of isotope tracers and nitrate dynamics

Xiaoqiang Yang[a,b,c*], Doerthe Tetzlaff[d,e,f], Junliang Jin[a,b,g], Qiongfang Li[a,b,h*], Dietrich Borchardt[i] and Chris Soulsby[f,d]

[a]The National Key Laboratory of Water Disaster Prevention, Hohai University, Nanjing, 210098, China

[b]Yangtze Institute for Conservation and Development, Hohai University, Nanjing, China

[c]Key Laboratory of Hydrologic-Cycle and Hydrodynamic-System of Ministry of Water Resources, Hohai University, Nanjing, China

[d]Department of Ecohydrology and Biogeochemistry, Leibniz Institute of Freshwater Ecology and Inland Fisheries (IGB), Berlin, Germany

[e]Department of Geography, Humboldt University of Berlin, Berlin, Germany

[f]Northern Rivers Institute, School of Geosciences, University of Aberdeen, Aberdeen, UK

[g]Research Center for Climate Change of Ministry of Water Resources, Nanjing 210029, China

[h]College of Hydrology and Water Resources, Hohai University, Nanjing, 210098, China

[i]Department of Aquatic Ecosystem Analysis and Management, Helmholtz Centre for Environmental Research – UFZ, Magdeburg, Germany

**Corresponding author: X.Yang (xq.yang@hhu.edu.cn); Q.Li (qfli@hhu.edu.cn)*

Highlights:

- A new space-time Damköhler (*Da*) framework based on coupled tracer-nitrate modeling
- *Da* reveals seasonal shifts from summer-processing to winter-transport dominance
- The upland arable areas are sensitive and impose pollution risks under drought
- The river-connected lowlands are processing hotspots and more resilient to drought
- *Da* space-time dynamics have implications for nature-based pollution control measures

Key words: space-time Damköhler framework, coupled modeling of tracers and nitrate, exposure and processing timescales, denitrification, catchment responses to drought, non-point source pollution control.

Abstract

Catchment-scale nitrate dynamics involve complex coupling of hydrological transport and biogeochemical transformations, imposing challenges for source control of diffuse pollution. The Damköhler number (*Da*) offers a dimensionless dual-lens concept that integrates the timescales of exposure and processing, but quantifying both timescales in heterogeneous catchments remains methodologically challenging. Here, we propose a novel spatio-temporal framework for catchment-scale quantification of *Da* based on the ecohydrological modeling platform EcH_2O-iso that coupled isotope-aided water age tracking and nitrate modeling. We examined *Da* variability of soil denitrification in the heterogeneous Selke catchment (456 km^2, central Germany). Results showed that warm-season soil denitrification was of catchment-wide significance (*Da* >1), while its high spatial variations were co-determined by varying exposure times and removal efficiencies (e.g., channel-connected lowland areas are hotspots). Moreover, *Da* seasonally shifted from processing-dominance to transport-dominance during the wet-spring season (from >1 to <1), implying important linkages between summer terrestrial denitrification and subsequent winter river water quality. Under the prolonged 2018-2019 droughts, denitrification removal generally reduced, resulting in further accumulation in agricultural soils. Moreover, the space-time responses of *Da* variability indicated important implications for catchment water quality. The older water in lowland areas exhibited extra risks of groundwater contamination, whilst agricultural areas in the hydrologically responsive uplands became sensitive hotspots for export and river water pollution. Importantly, the lowland pixels intersecting river channels exhibited high removal efficiencies, as well as high resilience to the disturbances (wet-spring *Da* shifted to >1 under drought conditions). The proposed catchment-wide Da framework is implied by mechanistic modeling, which is transferable across various environmental conditions. This could shed light on understanding of catchment N processes, and thus providing site-specific implications of non-point source pollution controls.

1 Introduction

Highly elevated nutrient levels in freshwaters are threatening the safe functioning of ecosystems and the provision of ecosystem services across extensive areas (Richardson et al., 2023). Further mitigations of such environmental problems focus on the difficult challenge of identifying and managing non-point sources, e.g., particularly under the prolonged droughts in Europe (Reusch et al., 2018; Yang et al., 2022). This inevitably requires advancing quantitative understanding of how catchment hydrology and biogeochemical processes interact and change. However, identifying and quantifying of complex transport-processing interactions at catchment scales remain fundamentally challenging (Abbott et al., 2016).

Several integrating frameworks have been proposed to explicitly characterize and classify transport-reaction interactions (Pinay et al., 2015). Amongst these, the widely used Damköhler number (Da) is defined as the ratio of exposure timescale (over which material has the opportunity to be processed) and processing timescale (the time for biogeochemical processes to reach equilibrium or substrate depletion) (Li et al., 2021; Oldham et al., 2013). Da is a dimensionless metric that is spatially and temporally scalable, and more uniquely, it quantitatively estimates the integration of nitrate transport and processing (Abbott et al., 2016). However, to quantify both timescales remains methodologically challenging. Current applications of the Da framework have been mostly restricted to steady-state groundwater systems or riparian/hyporheic zones (Ocampo et al., 2006). Catchment-scale applications are largely underexplored, particularly in terms of the space-time variability of Da (Oldham et al., 2013). Building on the process-specific feature of Da concepts, here we focus on terrestrial denitrification, because it is one of the dominant nitrate (NO_3^-) removal processes that influences catchment water quality (Pinay et al., 2015).

Acknowledging that hydrological processes are the first-order drivers of nutrient transport through catchment landscapes, some recent catchment water quality models have been developed based on advanced (eco-)hydrological platforms (Yang et al., 2018). However, many modeling platforms focus on simulating the celerity of hydrological responses and do not explicitly account for the velocities of water particles (Hrachowitz et al., 2016; McDonnell & Beven, 2014); consequently, the temporal dynamics of transport pathways affecting substances like NO_3^- and their exposure to biogeochemical transformations are either highly uncertain or not considered explicitly in water quality modeling. To address this fundamental celerity-velocity issue, stable isotopes of water (δ^2H and $\delta^{18}O$) are the most effective and popular natural tracers used in hydrology research (Abbott et al., 2016). In addition to the complementary role for improving model performance and process realism (Stadnyk & Holmes, 2023), isotope tracers can be used to infer catchment transit times and water ages, serving as a potential link between hydrology and water quality (Hrachowitz et al., 2016; Tunaley et al., 2016). Recent incorporation of isotopic tracers in fully distributed (eco-)hydrological platforms offers the potential for better representation of catchment heterogeneities in flow pathways and material transport. In particular, the tracer-aided ecohydrological model EcH_2O-iso (Kuppel et al., 2018; Maneta & Silverman, 2013) features a flux tracking module that takes the water age, together with δ^2H and $\delta^{18}O$, as generic tracers, thereby uniquely providing catchment-scale perspective of how water ages vary in storage and flux dynamics (Yang et al., 2023).

Based on the EcH_2O-iso model platform, this study proposed a model-based, catchment-scale *Da* integration framework. In addition to the isotope-aided water age tracking, we further coupled a process-based NO_3^- module developed by Yang et al. (2018). Specifically, considering the distributed N inputs (e.g., from agriculture activity), quantitative characteristics of NO_3^- residence and transport across the catchment were estimated from EcH_2O-iso hydrological states and fluxes. Meanwhile, the effective processing timescales of particular biogeochemical transformations were concurrently derived from simulations of the NO_3^- module. We examined the spatio-temporal *Da* integration of terrestrial denitrification in the data-rich, heterogenous Selke catchment (456 km^2, central Germany), where the high NO_3^- concentrations in surface water and groundwater are one of the major environmental concerns. This builds on earlier applications of EcH_2O-iso (Yang et al., 2021, 2023) and NO_3^- modeling (Yang et al., 2018) in this catchment, particularly the respective understanding of the catchment ecohydrological and NO_3^- dynamics under the disturbances of 2018-2019 droughts.

The overarching aims of this study were (a) to facilitate a fully distributed mechanistic catchment modeling framework that benefits from information from both conservative tracers and reactive nutrients, and (b) based on incorporation of *Da* concepts, to reveal the linkages between catchment biogeochemical processes (here the denitrification removal), hydrological transport and water quality. The specific research questions were:

(1) How to facilitate the coupled mechanistic modeling and to evaluate model performance based on multi-criteria calibrations?

(2) Based on the coupled modeling, how to quantify timescales of exposure and processing at catchment scales?

(3) What are the spatio-temporal patterns of *Da* variations and how they respond to drought disturbances?

The proposed model-based *Da* space-time analysis was anticipated to reveal landscape-scale "hot spots" and "hot moments" of NO_3^- removal via denitrification, as well as their impacts on catchment water quality. The insights would provide important implications for catchment pollution controls, especially under the changing environments.

2 Study area and data

2.1 The Selke catchment and monitoring networks

The Selke catchment (456 km^2) is located in central Germany (Figure 1a), with a transitional landscape from headwaters in the Harz Mountains to the lowland plain. Along with the elevation gradients (ranging from circa 600 m to 100 m), the catchment exhibits heterogenous hydro-climatic conditions. Annual precipitation decreases from 790 to 450 mm, and average annual temperature increases from 4.7 to 8.5 °C. The catchment geographic properties are also highly heterogenous (Figure 1b and c): the hilly uplands occupied mostly by forests with cambisols overlying shallow schist bedrock, while the flat lowland loess areas have long been intensively cultivated primarily due to the highly fertile chernozem soils. Major crops are rotated between winter wheat, winter rape-seed, and sugar beet, with typical N fertilizer applications of 175, 190, and 96 $kgN ha^{-1} yr^{-1}$, respectively (Yang et al., 2022).

The catchment is extensively equipped from multiple data monitoring initiatives (Figure 1a). The hydrology and water quality gauging stations on the main Selke River (Hausneindorf-HAUS, Meisdorf-MEIS and Silberhütte-SILB), are operated by the State Agency for Flood Protection and Water Management of Saxony-Anhalt (LHW) and Helmholtz-Centre for Environmental Research (UFZ). These nested stations capture dynamics of flow and riverine $NO_3^- - N$ concentrations from heterogeneous sub-areas. The monitoring of stable isotopes of water (δ^2H and $\delta^{18}O$) was conducted by UFZ (Department of Catchment Hydrology), and water samples were simultaneously taken from precipitation and stream water.

2.2 The multi-source data availability and pre-processing

Daily simulations were set-up for the study period during 2012-2020 (with 2010-2011 used as the model warm-up period). Meteorological observations were collected from the German Weather Service stations (DWD, https://opendata.dwd.de/climate_environment/CDC/, last accessed 22nd February, 2024) near the Selke catchment, including daily precipitation from 51 stations and daily meteorological elements (i.e., daily mean, maximum and minimum air temperature; daily wind speed, and relative humidity) from 15 stations. The spatial modeling resolution was set as 1 km × 1 km, and DWD meteorological data inputs were interpolated into this resolution as gridded inputs. Radiation data were retrieved from the ERA5 reanalysis with a resolution of 0.25°×0.25° (Hersbach et al., 2018), due to the limited DWD observations.

At the three gauging stations, daily discharge was collected directly from LHW (Figure 1d, https://gld.lhw-sachsen-anhalt.de/, last accessed 28th August, 2023). Continuous 15-min $NO_3^- - N$ concentrations has been collected using the ultraviolet spectral sensor OPUS (precision of 0.03 mgl^{-1} and accuracy of ±2%; TriOS, Germany), from which daily $NO_3^- - N$ concentrations were derived (Figure 1e). The isotope monitoring was conducted during 2012-2018, including monthly composite precipitation sampling at 27 sites in the larger Bode catchment (Lutz et al., 2018). All of these precipitation isotope data were spatio-temporally interpolated to derive the gridded daily inputs (1 km × 1 km). Seven precipitation sites located in the Selke catchment and their δ^2H isotope observations were presented in Figure 1a and 1d, respectively. The sampling points are mainly distributed in the upper mountainous part given the more heterogeneous climatic and landscape conditions, compared to the flat, homogeneous lowlands. Moreover, this study selected monthly grab sampled stream water isotopes from 5 sites (Figure 1d). Please refer to Yang et al. (2023) for detailed input data processing in the Selke catchment.

Figure 1 near here

Figure 1. The Selke catchment and the multi-source data monitoring. (a) monitoring network and DEM elevation above sea levels, (b) land covers, (c) soil types, (d) catchment average precipitation, discharge at the outlet HAUS and isotopes of precipitation and stream water samples at various sites, and (e) nitrate-nitrogen ($NO_3^- - N$) concentration observations at the three major gauging stations. Note that precipitation deuterium (δ^2H) values in (d) are shown as

monthly mean ± standard deviation among the 7 Selke sampling sites. Subplots (a), (b) and (c) are modified from Yang et al. (2023).

3 Method

3.1 The tracer-aided ecohydrological EcH_2O-iso model

The EcH_2O-iso model is process-based, tracer-aided ecohydrological model developed by Maneta & Silverman (2013) and Kuppel et al. (2018). In each of the grid cells, the model integrates modules of vertical energy balance, vertical and lateral water balance and vegetation dynamics (deactivated in this study). The energy balance is solved for each vegetation type at both canopy and land surface levels, from which evapotranspiration associated latent heat fluxes were calculated. Evaporation is considered at the canopy and top-layer soil and constrained by respective water storages. Plant transpiration is explicitly related to canopy conductance properties. The stomatal conductance is calculated using a Jarvis-type multiplicative model, and then upscaled to canopy conductance by leaf area index. The calculated transpiration flux is derived from root water uptake in three soil layers.

The water balance is conceptualized based on a bucket-type approach (Figure S1a for a schematic model structure). Vertical hydrological processes include precipitation, canopy interception, snowpack/snowmelt, surface infiltration and further infiltrating into three soil layers. A parsimonious conceptualization of deeper groundwater dynamics was added by Yang et al. (2021) to account for deeper baseflow sources. Lateral water exchanges between cells are considered as surface overland flow (from the surface ponding storage), subsurface interflow (from gravitational soil water drainage) and baseflow (from the deeper groundwater storage). Notably, EcH_2O-iso implements an independent river mask in accordance to the actual river network. This means only grid cells intersecting actual river channels (defined as channel-connected grid cells) contribute to runoff generations and channel routing (Figure S1a).

The flux-tracking module is fully integrated into the water balance component of the model (Kuppel et al., 2018). The generic tracer concentration is defined representing isotopic composition of δ^2H and $\delta^{18}O$, as well as water ages. In each water storage, a full mixing assumption is applied at the end of each time step. Thus, the outgoing fluxes have the same tracer signals as their source storages. Isotopic fractionation is considered in the upper soil layer based on the Craig-Gordon model (Craig & Gordon, 1965). Precipitation and throughfall enter into the system with the age of zero, and all ages increase by one time-step at end of each model time step. Detailed model descriptions and adaptations are referred to previous publications (Kuppel et al., 2018; Maneta & Silverman, 2013; Yang et al., 2021, 2023).

3.2 The catchment NO_3^- model and the denitrification calculation

We further loosely coupled EcH$_2$O-iso with catchment water quality modeling (particularly NO_3^-). The fully distributed EcH$_2$O-iso platform was adapted to account for the spatial variability in NO_3^- inputs (e.g., due to different agricultural activity). Moreover, EcH$_2$O-iso simulated water fluxes and state variables were used to drive NO_3^- transport and storage patterns across hydrological compartments (see Figure S1b). NO_3^- balances and conceptualizations of biogeochemical transformations were introduced from the work of Yang et al. (2018) and implementation in the Hydrological Predictions for the Environment-HYPE model (Lindström et al., 2010). Potential crop/plant N uptake is calculated using a three-parameter logistic growth function and partitioned into three soil layers according to root distributions. The actual uptake N amount is further constrained by soil water and N availability in each layer. N inputs from fertilizer/manure applications and plant residues are added to the top two layers (with the depth of 0~0.5 m). Four pools of soil N forms are defined for each soil layer, including dissolved pools of inorganic and organic nitrogen and solid pools of active and inactive organic nitrogen (Figure S1b). Terrestrial biogeochemical transformations are considered as denitrification removal, mineralization from organic to inorganic pools, dissolution equilibrium between dissolved and solid organic pools, and immobilization from inactive to active organic pools. In-stream nitrate-related transformations includes permanent removal via denitrification, temporary assimilatory uptake and the reverse re-mineralization.

As a process-based model, biogeochemical transformations are conceptualized according to the availability of sources and impacts of bio-environmental factors. The latter are often quantified in two ways: empirical functions for well-understood factors (e.g., temperature effects) and calibrated model parameters. For example, the amount of NO_3^- removed out of soil storage by the denitrification process, $R_D (kgNha^{-1}d^{-1})$, is calculated following the non-linear kinetics:

$$R_D = r_D \cdot f_{ST} \cdot f_{SM} \cdot f_{SMC} \cdot S_N \tag{1}$$

where r_D denotes the reaction rate as a model parameter (d^{-1}); S_N denotes the soil NO_3^- storage $(kgNha^{-1})$; f_{ST}, f_{SM} and f_{SMC} denote efficiency functions of soil temperature, soil moisture and soil $NO_3^- - N$ concentration, respectively (Lindström et al., 2010).

From previous modeling in the Selke catchment, large-scale EcH$_2$O-iso simulations are less successful at capturing isotopic signals in relatively wet years with higher influence of overland flow contributions (Yang et al., 2023). This is likely due to significant, but unknown, mixing between top-layer soil water and surface overland flow (Shi et al., 2011). Therefore, we parsimoniously introduced a mixing ratio (r_m, as a model parameter) to adjust the solute concentrations of surface overland flow: $r_m \cdot C_{tsoil} + (1 - r_m)C_{srf}$ (where C_{tsoil} and C_{srf} denote solute concentrations of the top-layer soil water and surface overland flow, respectively). This mixing adjustment was applied to both tracer and NO_3^- calculations.

3.3 Model parameterizations and the step-wise multi-criteria calibration

For the coupled modeling, the EcH$_2$O-iso parameters were assigned as either land cover or soil type dependent, and the nitrate module parameters were assigned as land cover type dependent and further simplified as agricultural and non-agricultural types. Sensitivity analysis has been previously conducted using the Morris method in the study catchment (Yang et al., 2018, 2023). Therefore, here we adapted the most sensitive parameters (listed in Table S1) and involved them in multi-criteria calibrations.

In accordance to the informal coupling strategy, the multi-criteria model calibrations were conducted step-wisely (see schematic diagram in Figure S2). The EcH$_2$O-iso model was firstly calibrated using the Monte Carlo based method (Ala-aho et al., 2017) against discharge and isotope observations from multiple sites, and the best 1000 runs were selected (out of 400 000 random sampling). Model performance metrics are Kling-Gupta Efficiency coefficient (KGE) and percentage bias (PBIAS) for discharge and Mean Absolute Error (MAE) for isotopes. Secondly, each of the 1000 EcH$_2$O-iso best runs was used to drive the NO_3^- module, and the Dynamically Dimensioned Search method (Tolson & Shoemaker, 2007) was used to calibrate parameters of the NO_3^- transformations. As such, the NO_3^- performance metrics were obtained accordingly (i.e., 1000 KGE values at each station). Finally, all of the 1000 metrics of discharge, isotopes and $NO_3^- - N$ concentrations were considered together to select the common best 100 runs. Details on the calibration methods and schemes are provided in Text S1 and Figure S2.

3.4 The model-based *Da* integration of the terrestrial denitrification process

The coupled mechanistic modeling provides explicit spatio-temporal information of age tracking and NO_3^- transformations, providing unique potential for a dual-lens analysis between hydrological and biogeochemical processes. The *Da* framework has been extensively used for the exposure-processing integration of specific processes, as following Oldham et al. (2013):

$$Da = \frac{\tau_E}{\tau_R} \tag{2}$$

where *Da* is the dimensionless Damköhler number; τ_E denotes the generalized exposure timescales and τ_R denotes the processing timescales. Specifically, when *Da*<1, NO_3^- transport is more dominated; when *Da*>1, NO_3^- will have plenty of opportunity to be denitrified.

As suggested by Oldham et al. (2013), this generalized *Da* concept can be applied to various regimes of advection- and diffusion-dominance, as well as hydrological disconnection. Thus, the modelled soil water ages are a proxy for residence times under various hydrological conditions; furthermore, they can be assumed to be equivalent to exposure times of dissolved NO_3^- to soil denitrifiers. For τ_R, we adopted the concept of effective processing timescale (i.e., derived from model or experimental fitting under various conditions(Oldham et al., 2013)), and used the calculation as follows:

$$\tau_R = (\frac{R_D}{S_N})^{-1} \tag{3}$$

where values of R_D and S_N (Eq. (1)) can be derived from the calibrated simulations. Note that the model calculated the above information separately for each soil layer. Thus, the whole-profile water ages were averaged with weights of each-layer water volumes, and both R_D and S_N were summed from all layers. Moreover, both τ_E and τ_R can be obtained for each model grid cell at each time step, thereby enabling an explicit spatio-temporal *Da* analysis.

4 Results

4.1 Performance of the coupled mechanistic modeling

Based on step-wise multi-criteria calibration, the model performances of discharge, isotopes and $NO_3^- - N$ concentrations were all reasonably good (Table 1 and Figures S3-S5). With overall KGEs ≥0.48 among all stations, discharge simulations captured the flow dynamics in terms of seasonal and inter-annual variability; particularly, the prolonged low-flows during the 2018-2019 droughts were reasonably reproduced (Figure S3). The isotope simulations also performed reasonably well at all sampling sites, with MAEs of δ^2H mostly < 4‰ at the upstream sites and around 6.5‰ at the outlet HAUS. The highly damped temporal patterns of stream water isotopes were also well reproduced; more importantly, the isotope-informed stream water age estimates exhibited seasonality and inter-annual variability that were consistent with catchment characteristics (Figure S4). For example, spring high-flows generally exhibited younger ages (≤ 1.0 year) than summer low-flows (3-4 years), and the normal years 2013-2017 exhibited much younger ages than the drought 2018-2019 (>5 years).

Driven by the EcH$_2$O-iso water fluxes, simulations of riverine $NO_3^- - N$ concentrations also performed well. The goodness-of-fit metrics were consistently good at all stations, with KGE and MAE means being > 0.50 and < 0.60 mgl^{-1}, respectively (Table 1). Moreover, the model nicely reproduced the observed seasonal patterns at each station (although missed some of the winter high values), as well as the upland-lowland differences (Figures 1e and S5). Particularly at the outlet HAUS, $NO_3^- - N$ concentrations exhibited complex changing patterns, representing dynamic loading contributions from the upper forested areas (gauged by the MEIS station) and the lowland intensive agricultural areas (where groundwater $NO_3^- - N$ concentration can be higher than 10 mgl^{-1}, from LHW measurements). Note that our simulations captured the increases of river $NO_3^- - N$ concentrations but notably underestimated the observed peaks during the wet season after the extreme drought in 2018 (Figure S5).

Table 1 near here

4.2 Spatio-temporal timescales of exposure and denitrification processing

The estimated soil water ages (i.e., the exposure times τ_E) showed high spatial variability (Figure 2). The upland forested mountains exhibited much younger ages than the lowland arable areas, primarily due to the upland-lowland hydro-climatic contrasts (i.e., semi-humid versus semi-arid climates and hilly-mountainous flashy versus low-gradient steady flow regimes (Dupas et al., 2017)). Moreover, the lowlands exhibited scattered spots with soil water ages >1500 days. The whole-profile averaged ages did not show significant seasonal differences (the ANOVA test p values > 0.1, Figure 2a-d). The soil water ages demonstrated different responses to the prolonged 2018-2019 droughts, though the upland-lowland contrasts were maintained (Figures 2e-h and 2i-l). In the uplands, the ages were extensively younger than the normal years during the wet (January-March) and drying seasons (April-Jun), primarily due to relatively higher soil water replenish rates after severe soil-water storage depletion under droughts; but the pattern shifted to be generally older than normal years during the dry (July-September) and drying seasons (October-December). The whole lowland areas showed age increases in all seasons, with the old-aged areas (>1500 days) exhibiting up to more than 500 days of increases. Moreover, the old-aged areas expended largely under droughts.

Figure 2 near here

Figure 2. Spatial distributions of profile-averaged soil water ages in different seasons in the normal years 2012-2017 (a-d), the drought years 2018-2019 (e-h), and their age differences (i-l). All values are based on the means of the best 100 runs, and the annotated values of mean ± standard deviation are derived from drainage areas above station MEIS (Upland) and between MEIS and HAUS (Lowland).

The denitrification processing time scales (τ_R) also exhibited spatio-temporal variations (Figures 3 and S6), while exhibiting less upland-lowland contrasts compared to denitrification removal rates (Figure S7) and soil NO_3^- stocks (Figure S8). In the normal years (Figures 3a and S6a), τ_R was the lowest during the warm seasons (July-October), which also exhibited the lowest spatial variance. This well indicated the strong denitrifying activity under less constraints of temperature and water conditions. Due to the seasonal cycling of the temperature constraint, catchment-wide τ_R increased to the highest in the coldest February and then starting to decrease as temperature increasing. Accordingly, the spatial variability of τ_R was enlarged (as indicated upland-lowland differences of means). Particularly, the lowland old-aged (Figure 2a-d) and channel-connected areas exhibited consistently low values and seasonal variations of τ_R, indicating more robust and active denitrification removal. The prolonged 2018-2019 droughts have induced substantial impacts, that τ_R increased substantially during the warm season throughout the catchment (Figures 3b-c and S6b-c). This is primarily caused by the largely reduced denitrify activity under strong water constraints (particularly in July-September, Figure S7b). The most dramatic changes occurred in the upland forests, which exhibited substantial τ_R increases since April, the beginning of the drought development. The impacts were further enlarged during the driest July-August (e.g., τ_R became mostly > 1500 days), coincident with the extremely decreased denitrification rates (almost by 100%, Figure S7c). In contrast, the upland agricultures exhibited much moderate τ_R increases throughout the warm season. The overall drought impacts were much relaxed from October as the catchment gets seasonally rewetted, and the τ_R during the wet season was relatively shorter than that of the normal years. This primarily due to the slightly stimulated denitrification, although the absolute rates were small (Figure S7b).

Figure 3 near here

Figure 3. Spatial distributions of monthly averaged processing times of soil denitrification (Eq. 3) during the normal years (a), the drought years (b) and their differences (c). Results of all 12 months are shown in Figure S6.

4.3 The spatio-temporal *Da* distributions and the changes under droughts

The integrated *Da* values exhibited high spatio-temporal variations, which also evolved differently in response to the prolonged droughts (Figures 4 and S9). In the normal years (Figures 4a and S9a), *Da* values were homogeneously >1 during the warm season when denitrification is mostly active. Moreover, the *Da* spatial distributions reflected both upland-lowland contrasts and the lowland variability, which are more in accordance to water ages (Figure 2) and processing times (Figure 3), respectively. The uplands exhibited relatively reduced *Da* ranges compared to the lowlands, and the latter exhibited areas with high *Da* values (i.e., reached up to >10 in old-aged and channel-connected areas), which were further consistently higher than other normal agricultural lowlands, where Da values were mostly less than 3. In general, obvious seasonal patterns were apparent, i.e., *Da* decreased during the rewetting November-December, gradually to be <1 during the wettest months, and then increased and shifted to be homogeneously >1 as the catchment becomes drying again. Notably, the timing of *Da* shifts was likely earlier in the lowlands than the uplands (e.g., after April and May, respectively, Figure S9).

The space-time *Da* distributions responded differently to the prolonged droughts (Figures 4b-c and S9b-c). The lowland *Da* showed a similar seasonal pattern to the normal years, while with decreased *Da* values during the driest July-September (Figure 4b-c). However, the upland *Da* emerged contrasting responses between the forests and the arable lands. The forests exhibited extended durations of *Da*<1, and particularly, *Da* exhibited shifts from the normal-year >1 to the drought-year <1 during warm seasons (Figures 4a-b and S9a-b), primarily due to higher increases of processing times than those of water ages (Figure 3c vs Figure 2j-k). However, *Da* in the upland agricultures continued to be >1, although they also decreased. In terms of relative *Da* changes (Figure 4c), there were catchment-wide decreases during the major drying-dry seasons (being directly impacted by the droughts), whereas increases were substantially observed during the relatively wet December-February.

Figure 4 near here

Figure 4. Spatial distributions of monthly averaged Damköhler number (*Da*) during the normal years (a) and the drought years (b), as well as *Da* relative changes (c). Results of all 12 months are shown in Figure S9.

5 Discussion

5.1 The coupled catchment modeling of conservative isotopes and reactive $NO_3^- - N$ dynamics

This study proposed a framework for fully distributed, mechanistic catchment modeling that couples tracer-aided ecohydrological and water quality simulations. The coupled modeling benefits from the advantages of the EcH_2O-iso model in terms of comprehensively representing the heterogeneity of catchment storage-flux interactions (Maneta & Silverman, 2013) and incorporating isotopic tracers for age tracking (Kuppel et al., 2018). Such methodological advances have been shown to be effective tools for constraining model performances in larger catchments (Smith et al., 2021; Yang et al., 2023). The seasonal patterns and inter-annual dynamics of discharge and stream isotopes (Section 4.1 and Figures S3 and S4) were in line with previous EcH_2O-iso modeling by Yang et al. (2023), who also explicitly demonstrated that the inclusion of isotopes in calibrations derives reasonable seasonal patterns of water ages (as shown in Figure S4). Notably, this study improved isotope performances during the wetter years of 2013-2014 (Table 1 and Figure S4) by parsimoniously considering the solute mixing between surface overland flow and top soil water (Shi et al., 2011). We acknowledge that such small-scale, non-linearity in overland flow and solute mixing are very challenging to be captured in larger-scale modeling (Yang et al., 2023). Future research needs to advance physical understanding at small scales and further address the scaling issues (Ke & Zhang, 2024). Moreover, more detailed isotope tracer or $NO_3^- - N$ data will be helpful to further constrain these processes at larger scales (e.g., using daily or sub-daily measurements for process conceptualization and parameter calibration).

Tracer-aided (eco-)hydrological modeling can provide more realistic runoff partitioning and internally consistent catchment storage-flux interactions (Stadnyk & Holmes, 2023). A more reliable basis for representing hydrological fluxes and storage states are an essential prerequisite for catchment reactive solute modeling, which superimposes complex biogeochemical processes for water quality simulations. Moreover, the fully distributed structure can accommodate spatial variability of NO_3^- inputs and relevant environmental factors. The overall performance of river $NO_3^- - N$ simulations was comparable to Yang et al. (2018), where NO_3^- dynamics are driven by a different hydrological model. Note that the observed spring concentration peaks after the drought 2018 were much-increased (up to 6.0 $mgNl^{-1}$), primarily due to the mobilization of further accumulated soil N from 2018 droughts (Winter et al., 2023). This is supported by our simulations of soil water concentrations in upland agricultural areas, which reached up to >7.0 $mgNl^{-1}$ in December 2018 (not shown), although the observed riverine high concentrations were missed. As an initial step of catchment integration of conservative and reactive solutes, this study adopted only loosely coupled models and the two-step calibration strategies (Section 3.3) to avoid time-consuming coding. We acknowledge that the nitrate model performance (particularly during winter and drought years) could be further improved if the information content of daily $NO_3^- - N$ data can be used to constrain flow dynamics under the high-flow and/or non-stationary drought conditions. Moreover, given the overall complexity of the coupled modeling system, future calibration efforts (e.g., considering the equifinality issue) should be advanced to improve the model performance and reliability.

5.2 Catchment-scale quantifications of nitrate exposure and processing timescales

One of the key objectives of this study was to address the challenges of applying *Da* concepts for heterogeneous, large-scale catchments (Kumar et al., 2020; Li et al., 2021). This study, for the first time, facilitated model-based inferences of both timescales and particularly focused on denitrification process and its impacts on catchment water quality.

Being fully integrated into water balance calculations, water ages of each storage and flux can be uniquely inferred from the EcH$_2$O-iso flux tracking (Kuppel et al., 2018; Smith et al., 2021; Yang et al., 2023). For the soil domain, the inferred soil water ages can be a proxy of residence times of soil water and NO_3^- solutes therein. Given the continuity in the modeling, this also provides an index for potential contact times for dissolved NO_3^- to be denitrified. Thus, the soil water ages fitted well to the concept of the exposure timescale (Frei & Peiffer, 2016; Oldham et al., 2013). More importantly, the fully distributed model structure enabled a spatial representation of the exposure times (Figure 2). Of course, the distributed exposure times can be explicitly inferred through particle tracking approaches (Frei & Peiffer, 2016), while to determine whether the biogeochemical turnover of interest is stimulated or suppressed along with the particle transport pathways will always remain challenging and highly uncertain for real systems (Frei & Peiffer, 2016). Therefore, we view the coupled-modeling approach, with Eulerian based flux tracking, used here to be a "middle-path" inference of the spatial exposure timescales.

Quantifying catchment-scale processing times of denitrification is even more challenging. First, natural catchment conditions are more complex than laboratory experiments that assume full exposure to reactants, thus the actual processing times could significantly differ from intrinsic processing times usually derived from the latter (Oldham et al., 2013). On the other hand, catchment models are advantageous in capturing the space-time variability of controlling environmental conditions of denitrification process, but they often do not explicitly simulate microbial dynamics (Boyer et al., 2006). Thus, the characteristic processing times cannot be inferred directly from kinetic theories (e.g., the common assumption of first-order kinetics). Here, we proposed an approach that directly estimates information of processing timescales using the modeled information (Eq. 3). The derived processing time represents the time it would take for denitrification rates to proceed to soil NO_3^- depletion at each time step (Li et al., 2021). The estimated space-time patterns of processing times (Figure 3) were reasonably in line to general understanding of denitrification characteristics (Seitzinger et al., 2006). Moreover, it is virtually equivalent to the inverse of denitrification removal efficiency, which has shown to be correlated to Da (Ocampo et al., 2006), thus it fitted well to the Da framework for catchment-scale integrated transport-processing analysis.

5.3 Space-time Da integrations of denitrification removal: insights into the linkages to catchment water quality and implications for management

Here we enabled explicit Da distributions throughout the catchment. Rather than the exact magnitudes of Da that may be more sensitive to model uncertainties (as discussed in Section 5.1), we were particularly interested in the space-time patterns of Da under different seasons and climatic conditions (Figures 4 and S9).

During conditions of normal-years between June-October, when denitrification is potentially most active, Da was consistently >1 (Figures 4a), supporting that the actual denitrification was significant in regulating catchment NO_3^- dynamics for both upland forests and lowland agricultural areas. Notably, the lowlands exhibited substantial areas with $Da \geq 5$, which are more extensive than the areas of older water (>1500 days in Figure 3); the emergent extra areas aligned well with locations of lowland channel network with relatively low processing times (Figures 2c-d, 3a and 4a). These low processing times were more due to the simulated year-round low soil NO_3^- stocks (Figure S8a). Such low stocks can be co-resulting from (1) the continuous supply of NO_3^- export to river channels (EcH$_2$O-iso only allows terrestrial exports from channel-connected grid cells) and (2) more active removal by denitrification especially during the wet-dry transition in May and November (Figure S7a). In the uplands, although exposure times were much shorter, Da values were homogeneously >1, with scattered high-values in non-channel forested areas (Figure 4a). Generally, the upland denitrification was strongly limited by soil NO_3^- sources availability (Dupas et al., 2017), resulting in much shorter processing times compared to the exposure times. However, once this source constraint was relaxed in agricultural areas, the significance of denitrification reduced, as reflected by slightly lower Da values compared to forests. In other words, these agricultural spots are potentially high-risk areas of NO_3^- accumulation; this further implies that agricultures could be NO_3^- export hotspots in such flashy uplands and should be cautiously managed, e.g., with reduced fertilizer applications and increased buffer space before exporting to rivers. Overall, the spatial variability of the warm-season *Da* values revealed that the significance of denitrification was not only reliant on sufficient exposure of NO_3^- to denitrifiers, but also the removal efficiency.

Due to the strong seasonality in both catchment hydrology and denitrifier activity, *Da* showed clear seasonal patterns (monthly averaged spatial distributions in Figures 4 and S9, and daily variations of typical grid-cells in Figure 5). The overall *Da* seasonal changes indicted the general shifting balance between NO_3^- processing (*Da*>1) and transport (*Da*<1) in dry summers and wet springs, respectively. Meanwhile, such seasonal shifts showed substantial spatial variations. First, the flashy uplands experienced a longer period of *Da*≤1 that persisted to May, while the lowland *Da* shifted to >1 in March (Figures 4a and 5). In other words, catchment NO_3^- transport during wet-spring seasons was of much more relevance in the uplands than the lowlands. This explains why the high NO_3^- loading (as well as riverine concentrations) during high-flow seasons are mostly contributed from the uplands (Figures S5), although the agricultural lowlands are extremely enriched in N. Second, in the homogeneous agricultural lowlands, *Da* showed contrasting seasonal variations that are also coincide with the warm-season spatial distributions. The high-*Da* areas with older soil water exhibited year-round *Da*>2, indicating a much lower influence of hydrological connectivity even during wet seasons. Compared to non-channel areas, lowland channel-connected areas exhibited consistently higher *Da* values (due to shorter processing times as shown in Figure 3a), forming year-round hot spots of denitrification removal.

Figure 5 near here

Figure 5. Averaged daily *Da* variations in various typical landscapes in the normal (2012-2017) and the drought (2018-2019) conditions. Two grid cells for each landscape type were selected and their locations were shown in Figure S10).

The prolonged droughts of 2018-2019 provided an opportunity to unravel catchment responses to climatic conditions that are expected to become more common in future (Figures 2e-h, 3b, 4b and dashed lines in Figure 5). During the warm seasons in the drought, the uplands experienced dramatic *Da* decreases, of which agricultures approached ~1 and forests shifted to ≪1. This is caused by the extremely depleted soil water availability (supported by local soil moisture data, as shown in Yang et al. (2021)), which constrained the anaerobic denitrification. Particularly for forests, the water constraints were superimposed on the source limitations, thereby resulting in extremely long processing times. The lowland also exhibited extensive *Da* decreases, indicating reduced dominance of removal processing due to denitrification being further water-limited. This resulted in extensive soil NO_3^- accumulations in lowland agricultures (Figure S8b). Moreover, it is likely that areas with high normal-year *Da* exhibited higher proportional decreases (e.g., more than 50% in the old-aged areas in July-September, Figure 5); consequently, these areas experienced more significant increases in soil stock (e.g., nearly doubled in November-December, Figure S8c). These drought sensitive "hot spots" are likely imposing high risks of groundwater contaminations, and thus are potential priorities for catchment management.

In addition, *Da* patterns during drought rewetting and wet seasons were largely maintained (i.e., *Da* generally reverted back to similar levels to those of normal years), indicating that catchment transport reestablished its dominance. This further means that the drought impacts on terrestrial denitrification would be eventually transmitted to river water quality. In fact, we did observe the elevated riverine $NO_3^- - N$ concentrations during January-March of drought years (ca. 6 $mgNl^{-1}$, Figure S5). Although the observed peak riverine concentrations were missed, the simulated soil water $NO_3^- - N$ concentrations of the upland agricultures reached to be >7.0 mgl^{-1} in 2018 December (results not shown), which would be flushed out to rivers during the following transport-dominant seasons. Therefore, the upland agricultural areas are particularly high-risk hot spots for high terrestrial NO_3^- exports under droughts. The lowland channel-connected areas exceptionally exhibited *Da* shifting to above 1 during January-February under droughts (Figure 5). This suggests that these areas not only exhibit high terrestrial denitrification removal efficiencies under normal conditions, but also prevent extra diffuse source exports under droughts, showing higher resilience to environmental changes. Moreover, these areas often associate with riparian/hyporheic zones, where the land-water interfaces are important biogeochemical hotspots benefiting catchment environments (Englund et al., 2021). This strongly implies that such a landscape type could play critical role on catchment environmental management under changing climates, and thus, promising pollution control measures could be to increase the lowland river connectivity with restored riparian wetlands.

6 Conclusion

Catchment-scale nutrient dynamics involve complex interactions between hydrology and biogeochemistry, thus requiring a dual-lens approach that integrates both exposure and processing timescales. Using *Da* concepts, this study proposed a novel spatio-temporal framework for *Da* quantification in relation to soil denitrification based on a coupled mechanistic modeling of isotope-aided water age tracking and NO_3^- turnover. The *Da* values revealed the general significance of denitrifying activity during dry-summer seasons, and particular hot spots included agricultural areas in the flashy uplands and channel-connected areas in the flat lowlands. Moreover, *Da* seasonal patterns demonstrated a systematic shift to transport dominance during wet-spring seasons, implying that terrestrial denitrification impacts on river water quality are mediated by hydrological connectivity. Importantly, the space-time changes of *Da* under droughts helped identify high-risk “hot spots” of catchment water pollution whilst also identifying less-sensitive areas exhibiting high resilience to environmental changes. These insights into integrated hydrological and biogeochemical dynamics have important implications for modern nature-based catchment non-point source pollution control, e.g., through implementing buffer zones in risky uplands to prevent high N-export and increasing lowland river connectivity with restored riparian wetlands along lowland rivers to increase biogeochemical N removal. In addition, the proposed catchment *Da* framework is methodologically transferable to other processes of interest and to other regions under various climate and landscape conditions.

Acknowledgement

The authors thank Michael Rode, Kay Knöller, Ralf Merz and Christin Müller for the isotope data. X.Y. is partly supported by “the Fundamental Research Funds for the Central Universities” and the National Key Laboratory of Water Disaster Prevention (Grant No. 524015292, 2020490211）. The German Weather Service, the Federal Agency for Cartography and Geodesy and the State Agency for Flood Protection and Water Management (Saxony-Anhalt) are acknowledged for data support.

References

Abbott, B. W., Baranov, V., Mendoza-Lera, C., Nikolakopoulou, M., Harjung, A., Kolbe, T., et al. (2016). Using multi-tracer inference to move beyond single-catchment ecohydrology. *Earth-Science Reviews*, *160*, 19–42. https://doi.org/10.1016/j.earscirev.2016.06.014

Ala-aho, P., Tetzlaff, D., McNamara, J. P., Laudon, H., & Soulsby, C. (2017). Using isotopes to constrain water flux and age estimates in snow-influenced catchments using the STARR (Spatially distributed Tracer-Aided Rainfall–Runoff) model. *Hydrol. Earth Syst. Sci.*, *21*(10), 5089–5110. https://doi.org/10.5194/hess-21-5089-2017

Boyer, E. W., Alexander, R. B., Parton, W. J., Li, C., Butterbach-Bahl, K., Donner, S. D., et al. (2006). Modeling Denitrification in Terrestrial and Aquatic Ecosystems at Regional Scales. *Ecological Applications*, *16*(6), 2123–2142. https://doi.org/10.1890/1051-0761(2006)016[2123:MDITAA]2.0.CO;2

Craig, H., & Gordon, L. I. (1965). Deuterium and Oxygen 18 variations in the ocean and the marine atmosphere. In *Stable isotopes in Oceanographic studies and paleotemperatures*. Pisa: Laboratorio di geologia numcleare.

Dupas, R., Musolff, A., Jawitz, J. W., Rao, P. S. C., Jäger, C. G., Fleckenstein, J. H., et al. (2017). Carbon and nutrient export regimes from headwater catchments to downstream reaches. *Biogeosciences*, *14*(18), 4391–4407. https://doi.org/10.5194/bg-14-4391-2017

Englund, O., Börjesson, P., Mola-Yudego, B., Berndes, G., Dimitriou, I., Cederberg, C., & Scarlat, N. (2021). Strategic deployment of riparian buffers and windbreaks in Europe can co-deliver biomass and environmental benefits. *Communications Earth & Environment*, *2*(1), 1–18. https://doi.org/10.1038/s43247-021-00247-y

Frei, S., & Peiffer, S. (2016). Exposure times rather than residence times control redox transformation efficiencies in riparian wetlands. *Journal of Hydrology*, *543*, 182–196. https://doi.org/10.1016/j.jhydrol.2016.02.001

Hersbach, H., Bell, B., Berrisford, P., Biavati, G., Horányi, A., Muñoz Sabater, J., et al. (2018). ERA5 hourly data on pressure levels from 1979 to present. Copernicus Climate Change Service (C3S) Climate Data Store (CDS). https://doi.org/10.24381/cds.bd0915c6

Hrachowitz, M., Benettin, P., van Breukelen, B. M., Fovet, O., Howden, N. J. K., Ruiz, L., et al. (2016). Transit times—the link between hydrology and water quality at the catchment scale. *Wiley Interdisciplinary Reviews: Water*, *3*(5), 629–657. https://doi.org/10.1002/wat2.1155

Ke, Q., & Zhang, K. (2024). Scale issues in runoff and sediment delivery (SIRSD): A systematic review and bibliometric analysis. *Earth-Science Reviews*, *251*, 104729. https://doi.org/10.1016/j.earscirev.2024.104729

Kumar, R., Heße, F., Rao, P. S. C., Musolff, A., Jawitz, J. W., Sarrazin, F., et al. (2020). Strong hydroclimatic controls on vulnerability to subsurface nitrate contamination across Europe. *Nature Communications*, *11*(1), 6302. https://doi.org/10.1038/s41467-020-19955-8

Kuppel, S., Tetzlaff, D., Maneta, M. P., & Soulsby, C. (2018). EcH2O-iso 1.0: water isotopes and age tracking in a process-based, distributed ecohydrological model. *Geosci. Model Dev.*, *11*(7), 3045–3069. https://doi.org/10.5194/gmd-11-3045-2018

Li, L., Sullivan, P. L., Benettin, P., Cirpka, O. A., Bishop, K., Brantley, S. L., et al. (2021). Toward catchment hydro-biogeochemical theories. *Wiley Interdisciplinary Reviews: Water*, *8*(1), e1495. https://doi.org/10.1002/wat2.1495

Lindström, G., Pers, C., Rosberg, J., Strömqvist, J., & Arheimer, B. (2010). Development and testing of the HYPE (Hydrological Predictions for the Environment) water quality model for different spatial scales. *Hydrology Research*, *41*(3–4), 295–319. https://doi.org/10.2166/nh.2010.007

Lutz, S. R., Krieg, R., Müller, C., Zink, M., Knöller, K., Samaniego, L., & Merz, R. (2018). Spatial Patterns of Water Age: Using Young Water Fractions to Improve the Characterization of Transit Times in Contrasting Catchments. *Water Resources Research*, *54*(7), 4767–4784. https://doi.org/10.1029/2017WR022216

Maneta, M. P., & Silverman, N. L. (2013). A Spatially Distributed Model to Simulate Water, Energy, and Vegetation Dynamics Using Information from Regional Climate Models. *Earth Interactions*, *17*(11), 1–44. https://doi.org/10.1175/2012ei000472.1

McDonnell, J. J., & Beven, K. (2014). Debates—The future of hydrological sciences: A (common) path forward? A call to action aimed at understanding velocities, celerities and residence time distributions of the headwater hydrograph. *Water Resources Research*, *50*(6), 5342–5350. https://doi.org/10.1002/2013WR015141

Ocampo, C. J., Oldham, C. E., & Sivapalan, M. (2006). Nitrate attenuation in agricultural catchments: Shifting balances between transport and reaction. *Water Resources Research*, *42*(1). https://doi.org/10.1029/2004WR003773

Oldham, C. E., Farrow, D. E., & Peiffer, S. (2013). A generalized Damköhler number for classifying material processing in hydrological systems. *Hydrology and Earth System Sciences*, *17*(3), 1133–1148. https://doi.org/10.5194/hess-17-1133-2013

Pinay, G., Peiffer, S., De Dreuzy, J.-R., Krause, S., Hannah, D. M., Fleckenstein, J. H., et al. (2015). Upscaling Nitrogen Removal Capacity from Local Hotspots to Low Stream Orders' Drainage Basins. *Ecosystems*, *18*(6), 1101–1120. https://doi.org/10.1007/s10021-015-9878-5

Reusch, T. B. H., Dierking, J., Andersson, H. C., Bonsdorff, E., Carstensen, J., Casini, M., et al. (2018). The Baltic Sea as a time machine for the future coastal ocean. *Science Advances*, *4*(5). https://doi.org/10.1126/sciadv.aar8195

Richardson, K., Steffen, W., Lucht, W., Bendtsen, J., Cornell, S. E., Donges, J. F., et al. (2023). Earth beyond six of nine planetary boundaries. *Science Advances*, *9*(37), eadh2458. https://doi.org/10.1126/sciadv.adh2458

Seitzinger, S., Harrison, J. A., Böhlke, J. K., Bouwman, A. F., Lowrance, R., Peterson, B., et al. (2006). Denitrification across landscapes and waterscapes: A synthesis. *Ecological Applications*, *16*(6), 2064–2090. https://doi.org/10.1890/1051-0761(2006)016[2064:DALAWA]2.0.CO;2

Shi, X., Wu, L., Chen, W., & Wang, Q. (2011). Solute Transfer from the Soil Surface to Overland Flow: A Review. *Soil Science Society of America Journal*, *75*(4), 1214–1225. https://doi.org/10.2136/sssaj2010.0433

Smith, A., Tetzlaff, D., Kleine, L., Maneta, M., & Soulsby, C. (2021). Quantifying the effects of land use and model scale on water partitioning and water ages using tracer-aided ecohydrological models. *Hydrol. Earth Syst. Sci.*, *25*(4), 2239–2259. https://doi.org/10.5194/hess-25-2239-2021

Stadnyk, T. A., & Holmes, T. L. (2023). Large scale hydrologic and tracer aided modelling: A review. *Journal of Hydrology*, *618*, 129177. https://doi.org/10.1016/j.jhydrol.2023.129177

Tolson, B. A., & Shoemaker, C. A. (2007). Dynamically dimensioned search algorithm for computationally efficient watershed model calibration. *Water Resources Research*, *43*(1). https://doi.org/10.1029/2005WR004723

Tunaley, C., Tetzlaff, D., Lessels, J., & Soulsby, C. (2016). Linking high-frequency DOC dynamics to the age of connected water sources. *Water Resources Research*, *52*(7), 5232–5247. https://doi.org/10.1002/2015WR018419

Winter, C., Nguyen, T. V., Musolff, A., Lutz, S. R., Rode, M., Kumar, R., & Fleckenstein, J. H. (2023). Droughts can reduce the nitrogen retention capacity of catchments. *Hydrology and Earth System Sciences*, *27*(1), 303–318. https://doi.org/10.5194/hess-27-303-2023

Yang, X., Jomaa, S., Zink, M., Fleckenstein, J. H., Borchardt, D., & Rode, M. (2018). A new fully distributed model of nitrate transport and removal at catchment scale. *Water Resources Research*, *54*(8), 5856–5877. https://doi.org/10.1029/2017WR022380

Yang, X., Tetzlaff, D., Soulsby, C., Smith, A., & Borchardt, D. (2021). Catchment Functioning Under Prolonged Drought Stress: Tracer-Aided Ecohydrological Modeling in an Intensively Managed Agricultural Catchment. *Water Resources Research*, *57*(3), e2020WR029094. https://doi.org/10.1029/2020WR029094

Yang, X., Rode, M., Jomaa, S., Merbach, I., Tetzlaff, D., Soulsby, C., & Borchardt, D. (2022). Functional Multi-Scale Integration of Agricultural Nitrogen-Budgets Into Catchment Water Quality Modeling. *Geophysical Research Letters*, *49*(4), e2021GL096833. https://doi.org/10.1029/2021GL096833

Yang, X., Tetzlaff, D., Müller, C., Knöller, K., Borchardt, D., & Soulsby, C. (2023). Upscaling Tracer-Aided Ecohydrological Modeling to Larger Catchments: Implications for Process Representation and Heterogeneity in Landscape Organization. *Water Resources Research*, *59*(3), e2022WR033033. https://doi.org/10.1029/2022WR033033

Figure 1

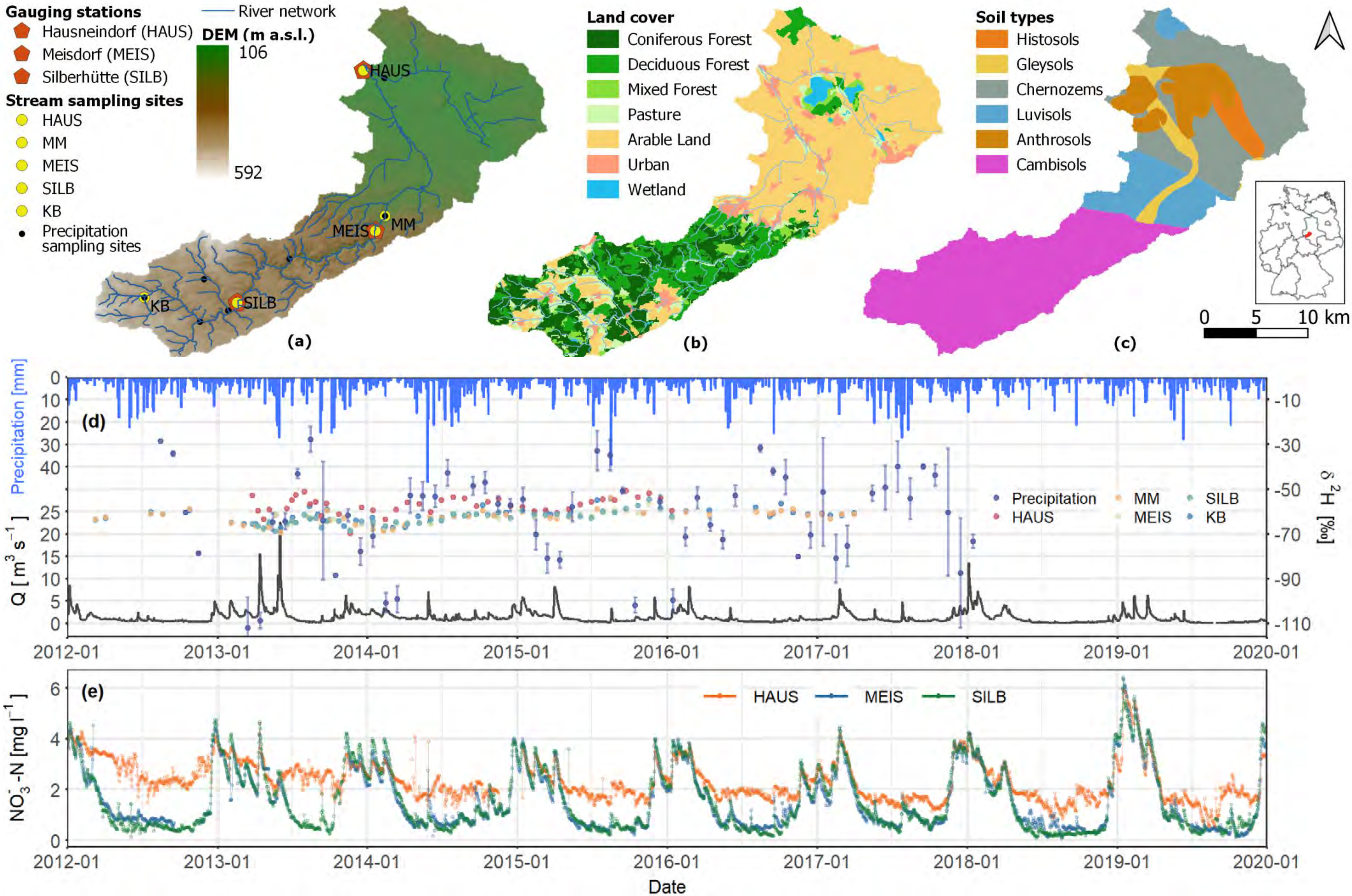

Gauging stations
Hausneindorf (HAUS)
Meisdorf (MEIS)
Silberhütte (SILB)
Stream sampling sites
HAUS
MM
MEIS
SILB
KB
Precipitation sampling sites
River network
DEM (m a.s.l.)
106
592
HAUS
MEIS
MM
SILB
KB
(a)
Land cover
Coniferous Forest
Deciduous Forest
Mixed Forest
Pasture
Arable Land
Urban
Wetland
(b)
Soil types
Histosols
Gleysols
Chernozems
Luvisols
Anthrosols
Cambisols
0
5
10 km
(c)
Precipitation [mm]
(d)
Q [m³ s⁻¹]
δ ²H [‰]
Precipitation
HAUS
MM
MEIS
SILB
KB
(e)
NO₃⁻-N [mg l⁻¹]
HAUS
MEIS
SILB
2012-01
2013-01
2014-01
2015-01
2016-01
2017-01
2018-01
2019-01
2020-01
Date

Figure 2

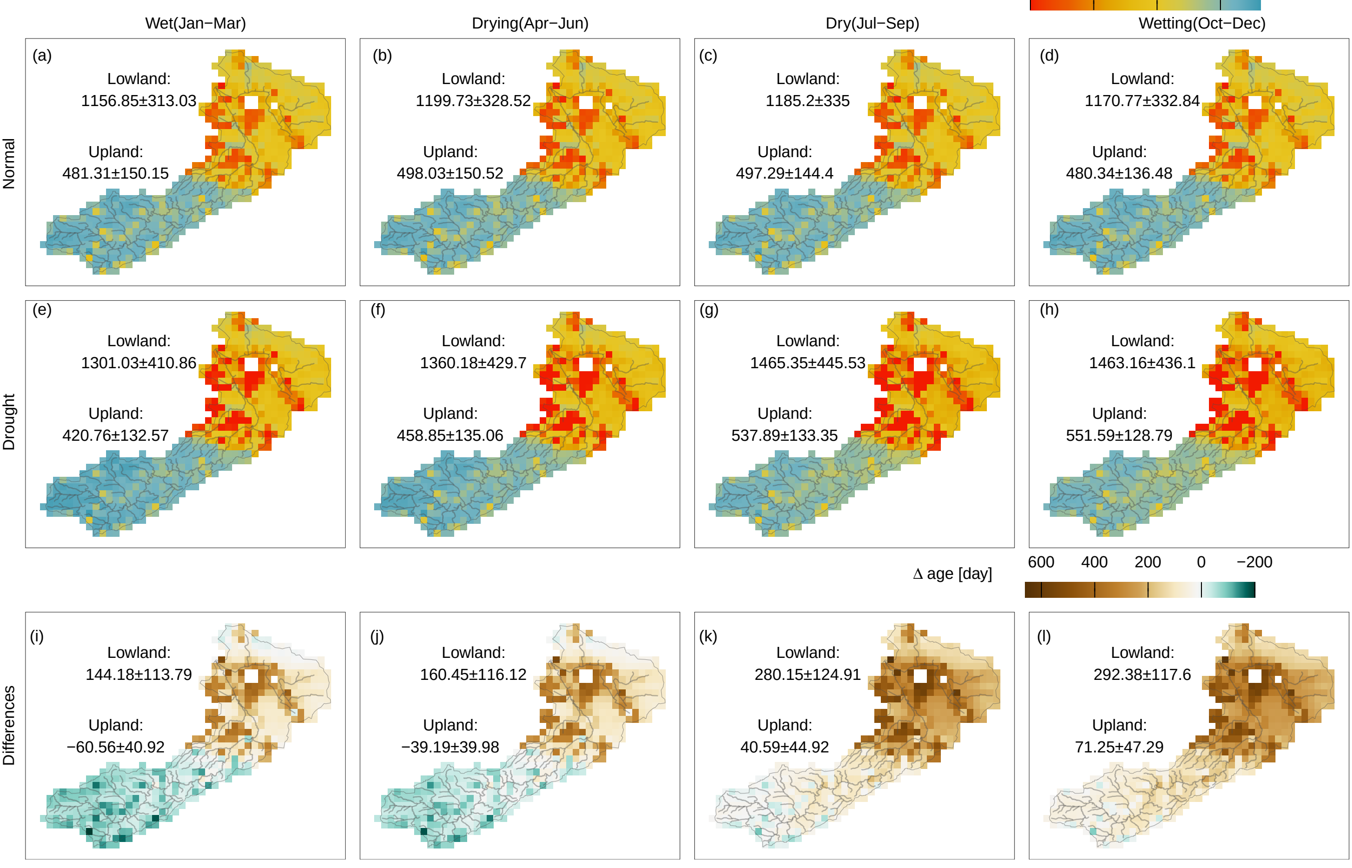

Age [day]
>2000
1500
1000
500
Wet(Jan−Mar)
Drying(Apr−Jun)
Dry(Jul−Sep)
Wetting(Oct−Dec)
Normal
(a)
Lowland:
1156.85±313.03
Upland:
481.31±150.15
(b)
Lowland:
1199.73±328.52
Upland:
498.03±150.52
(c)
Lowland:
1185.2±335
Upland:
497.29±144.4
(d)
Lowland:
1170.77±332.84
Upland:
480.34±136.48
Drought
(e)
Lowland:
1301.03±410.86
Upland:
420.76±132.57
(f)
Lowland:
1360.18±429.7
Upland:
458.85±135.06
(g)
Lowland:
1465.35±445.53
Upland:
537.89±133.35
(h)
Lowland:
1463.16±436.1
Upland:
551.59±128.79
Δ age [day]
600
400
200
0
−200
Differences
(i)
Lowland:
144.18±113.79
Upland:
−60.56±40.92
(j)
Lowland:
160.45±116.12
Upland:
−39.19±39.98
(k)
Lowland:
280.15±124.91
Upland:
40.59±44.92
(l)
Lowland:
292.38±117.6
Upland:
71.25±47.29

Figure 3

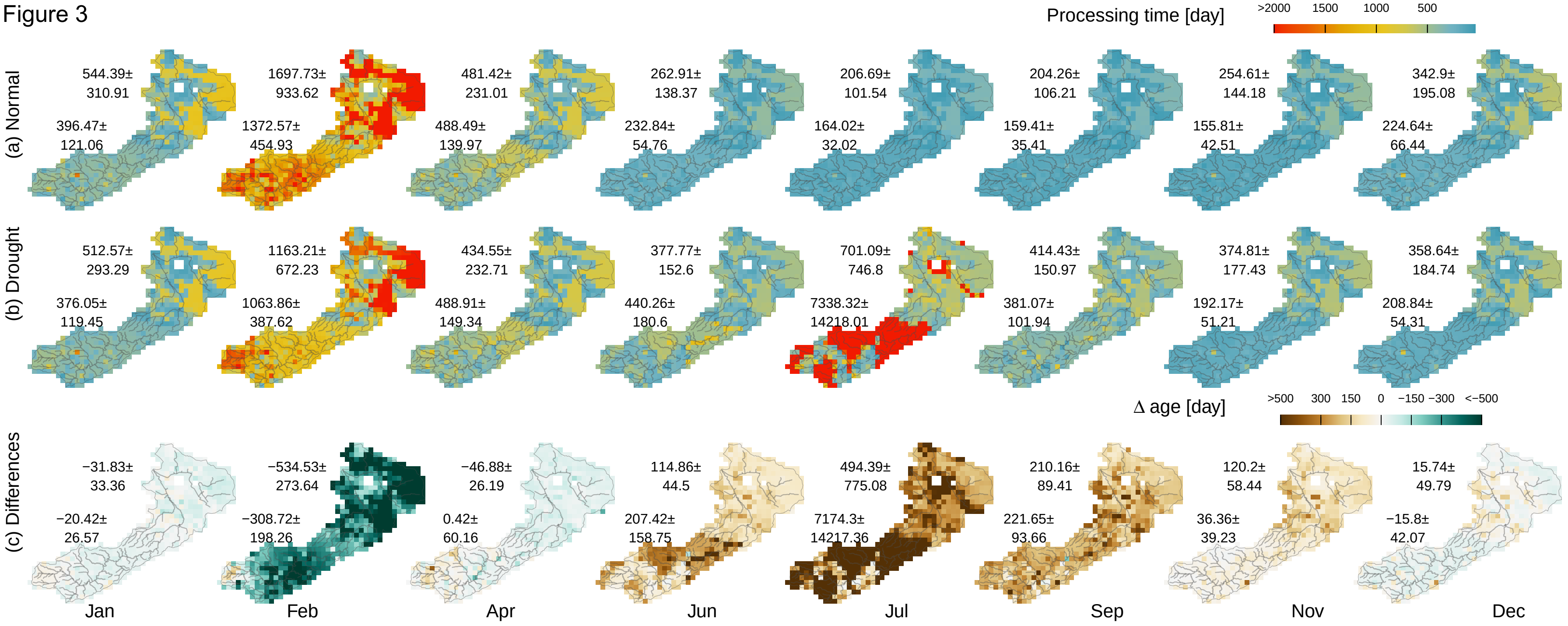
Processing time [day]
>2000
1500
1000
500
(a) Normal
544.39±
310.91
396.47±
121.06
1697.73±
933.62
1372.57±
454.93
481.42±
231.01
488.49±
139.97
262.91±
138.37
232.84±
54.76
206.69±
101.54
164.02±
32.02
204.26±
106.21
159.41±
35.41
254.61±
144.18
155.81±
42.51
342.9±
195.08
224.64±
66.44
(b) Drought
512.57±
293.29
376.05±
119.45
1163.21±
672.23
1063.86±
387.62
434.55±
232.71
488.91±
149.34
377.77±
152.6
440.26±
180.6
701.09±
746.8
7338.32±
14218.01
414.43±
150.97
381.07±
101.94
374.81±
177.43
192.17±
51.21
358.64±
184.74
208.84±
54.31
Δ age [day]
>500
300
150
0
−150
−300
<−500
(c) Differences
−31.83±
33.36
−20.42±
26.57
−534.53±
273.64
−308.72±
198.26
−46.88±
26.19
0.42±
60.16
114.86±
44.5
207.42±
158.75
494.39±
775.08
7174.3±
14217.36
210.16±
89.41
221.65±
93.66
120.2±
58.44
36.36±
39.23
15.74±
49.79
−15.8±
42.07
Jan
Feb
Apr
Jun
Jul
Sep
Nov
Dec

Figure 4

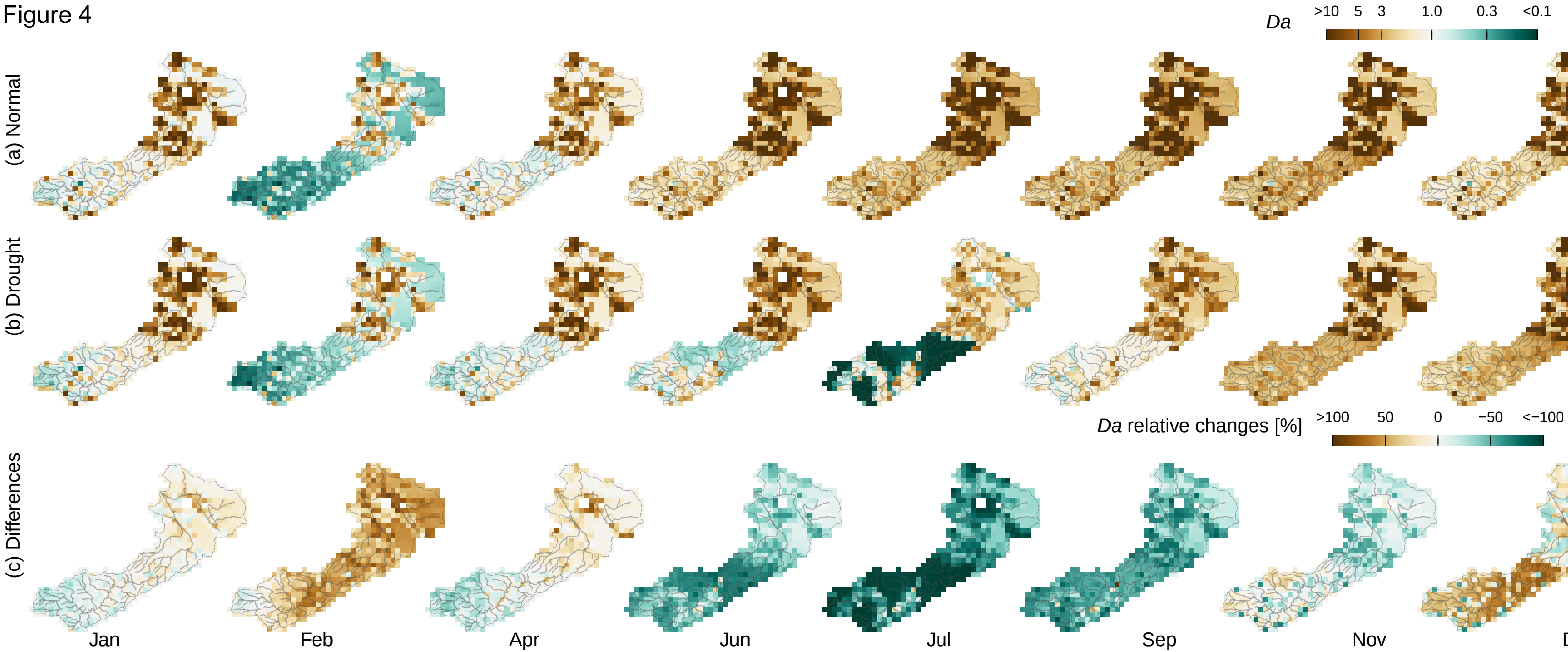
Da
>10 5 3 1.0 0.3 <0.1
(a) Normal
(b) Drought
Da relative changes [%]
>100 50 0 −50 <−100
(c) Differences
Jan
Feb
Apr
Jun
Jul
Sep
Nov
Dec

Figure 5

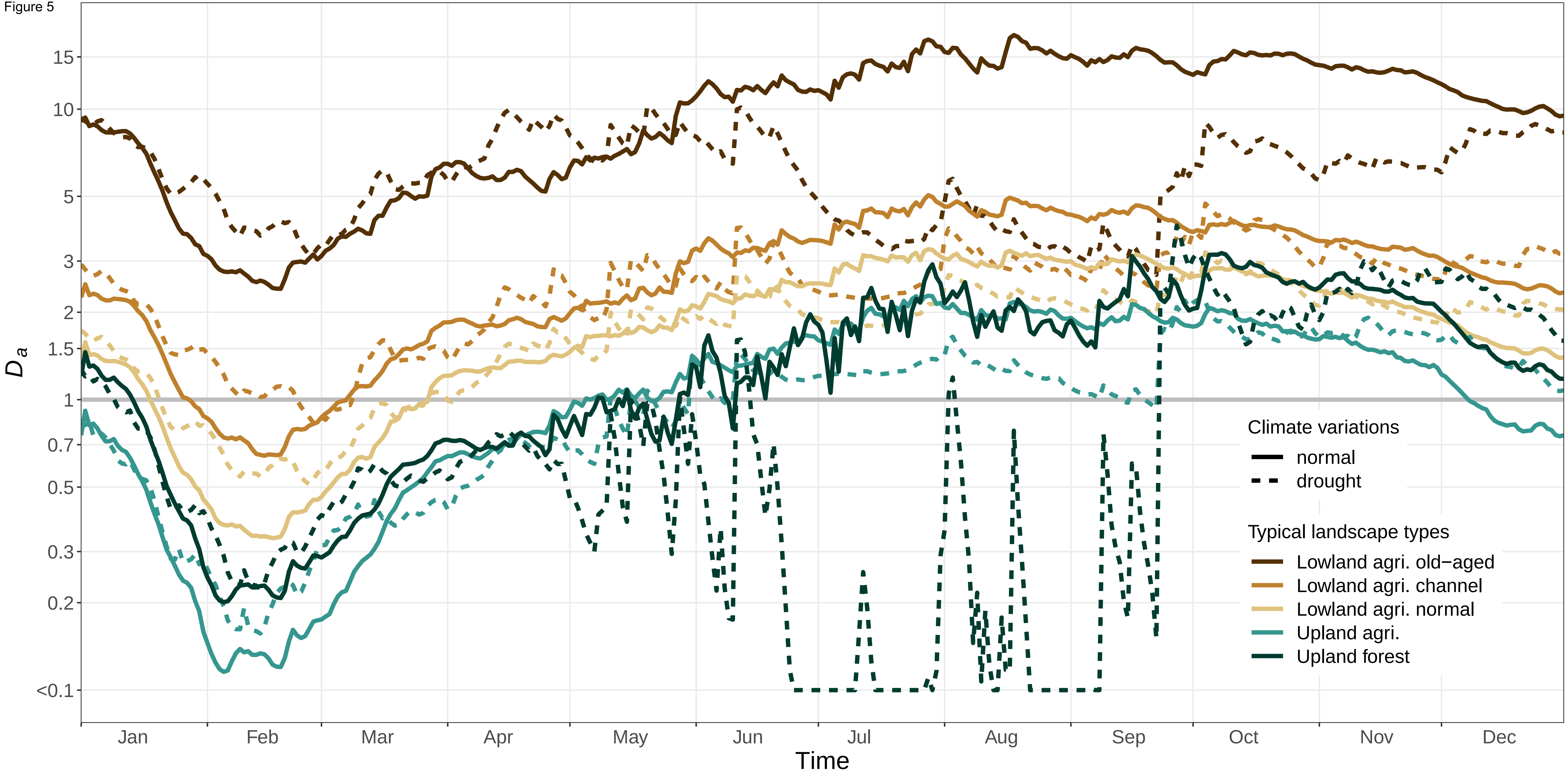

15
10
5
3
2
1.5
1
0.7
0.5
0.3
0.2
<0.1
D_a
Jan
Feb
Mar
Apr
May
Jun
Jul
Aug
Sep
Oct
Nov
Dec
Time
Climate variations
normal
drought
Typical landscape types
Lowland agri. old−aged
Lowland agri. channel
Lowland agri. normal
Upland agri.
Upland forest

Table 1. The coupled model performance based on the multi-criteria, multi-site calibrations. Mean ± Standard Deviation values were calculated among the best 100 runs. KGE – Kling Gupta Efficiency, PBIAS and MAE – the mean percentage bias and mean absolute errors, respectively, between the simulations and observations.

Data type	Metric	HAUS	MEIS	SILB	MM	KB
Discharge	KGE [-]	0.48±0.056	0.52±0.076	0.69±0.051	--	--
	PBIAS [%]	22.78±9.06	17.91±9.19	15.54±8.54	--	--
Isotope $\delta^2 H$	MAE [‰]	6.44±0.64	2.93±0.36	3.11±0.38	3.08±0.28	3.87±0.36
$NO_3^- - N$ concentration	KGE [-]	0.52±0.049	0.57±0.060	0.64±0.044	--	--
	MAE $[mgl^{-1}]$	0.53±0.056	0.58±0.045	0.60±0.048	--	--